Panoramic quantitative phase imaging of adherent live cells in a microfluidic environment

YING MA,[1,2,3,†] TAIQIANG DAI,[4,†] YUNZE LEI,[1,2,3,†] LINLIN ZHANG,[4] LIN MA,[1,2,3] MIN LIU,[1,2,3] SHA AN,[1,2,3] JUANJUAN ZHENG,[1,2,3] KEQUN ZHUO,[1,2,3] LIANG KONG,[4,5,‡] AND PENG GAO[1,2,3,6,‡]

[1]*School of Physics, Xidian University, Xi'an 710071, China*
[2]*Key Laboratory of Optoelectronic Perception of Complex Environment, Ministry of Education, China*
[3]*Engineering Research Center of Functional Nanomaterials, Universities of Shaanxi Province, China*
[4]*State Key Laboratory of Military Stomatology & National Clinical Research Center for Oral Diseases & Shaanxi Engineering Research Center for Dental Materials and Advanced Manufacture, School of Stomatology, The Fourth Military Medical University, Xi'an 710000, China*
[5]*liangkong2014@163.com*
[6]*peng.gao@xidian.edu.cn*
[†]Contributed equally
[‡]Co-corresponding authors

Abstract: Understanding how cells respond to external stimuli is crucial. However, there are a lack of inspection systems capable of simultaneously stimulating and imaging cells, especially in their natural states. This study presents a novel microfluidic stimulation and observation system equipped with flat-fielding quantitative phase contrast microscopy (FF-QPCM). This system allowed us to track the behavior of organelles in live cells experiencing controlled microfluidic stimulation. Using this innovative imaging platform, we successfully quantified the cellular response to shear stress including directional cellular shrinkage and mitochondrial distribution change in a label-free manner. Additionally, we detected and characterized the cellular response, particularly mitochondrial behavior, under varying fluidic conditions such as temperature and drug induction time. The proposed imaging platform is highly suitable for various microfluidic applications at the organelle level. We advocate that this platform will significantly facilitate life science research in microfluidic environments.

1. Introduction

Live cells often exhibit functional and morphological changes in response to physical or chemical stimuli, which can be reflected in subcellular organelles. Cell morphology observation and organelle analysis are crucial for understanding the underlying mechanisms behind various life phenomena. One common approach to controlling the microenvironment of live cells is by using microfluidic chip systems [1,2]. For instance, Mao et al. developed a fluid cell knife by open microfluidics for wound repair study and organelle transport analysis [3]. Zhang et al. reported a diamond shaped microfluidic device to study the shear effects of heterogeneous hemodynamic patterns in the onset and progression of various vascular diseases [4]. Yang et al. proposed a passive pump-assisted microfluidic assay for quantifying endothelial wound healing in response to fluid shear stress [5]. Garud et al. demonstrated a hybrid approach of computational fluid dynamics and Taguchi analysis to establish a microfluidic cerebrovascular model based on the effect of various influential factors on the shear stress [6]. And Na et al. developed a microfluidic system for precisely reproducing physiological blood pressure and wall shear stress to endothelial cells [7]. It is undeniable that the study of the effect of shear stress on life activities by means of microfluidic chips is currently only confined to the cellular and even tissue level. Microfluidic

cell analysis technologies have rapidly evolved in recent years and have become powerful tools in cell biology research and analysis [8,9].

Diverse fluorescence microscopic technologies, such as wide-field fluorescence microscopy, 3D fluorescence microscopy, confocal laser scanning microscopy, and laser-excited fluorescence lifetime, have been integrated with specially designed microfluidic chips bio-sensing [10–15]. Wide-field fluorescence microscopy has been integrated with dynamic microfluidic cytometry to capture the G-protein-coupled receptor signaling [11]. It has also been equipped with a multichannel synchronous hydrodynamic gating device to investigate adenosine triphosphate (ATP) and histamine (HA) responses in Hela cells [12]. In another study, wide-field fluorescence microscopy was used to capture quasi-3D cytoskeletal dynamics of osteocytes under shear stress by incorporating a 45° mirror into the light path [13]. Recently, more advanced fluorescent imaging systems and analysis methods have been employed to obtain detailed information about cells in microenvironments. For example, confocal laser scanning microscopy was coupled with a drop-based microfluidic device to determine single-cell bacterial physiology and to directly measure shear strain in adherent vascular endothelial cells exposed to fluid shear stress [14]. Moreover, laser-excited fluorescence lifetime imaging was utilized to quantify antibody binding kinetics on various biological substrates [15]. It is worth noting that microfluidic cell analysis based on fluorescence imaging is subject to photobleaching and phototoxicity to some extent.

Compared to the fluorescence imaging techniques, quantitative phase microscopy (QPM) has experienced rapid development in recent years due to its unique advantages of label-free detection, affordability, and non-invasiveness, making it an important tool in life science research [16,17] and industrial testing [18]. QPM has also some limitations, such as computational complexity, lack of specificity, and moderate spatial resolution (below the diffraction limit). Nevertheless, being a label-free, high resolution and high contrast imaging technique, QPM has been developed in diverse ways and they have important application value [19–26]. To name only a few, optical diffraction tomography (ODT) based on annular mechanical scanning illumination has rendered the refractive index (RI) distribution of cells and internal organelles with high spatial resolution [20,21]. Gradient light interference microscopy (GLIM) [22] and spatial light interference microscopy (SLIM) [23,24] allows visualization of thick embryos and subtle organelles with high quality. Fourier ptychographic microscopy (FPM)-based computational adaptive optical method has secured the high-quality performance for long-term imaging across a wide field [25]. Further, scan-free intensity diffraction tomography technique utilizing annular illumination can rapidly characterize large-volume three-dimensional refractive index distributions in vitro [26]. The potential of QPM has been further realized by incorporating microfluidic devices into QPM imaging systems to support or transport samples. For instance, off-axis digital holography microscopy (DHM) has been used to analyze the elastography of whole-cell shear stiffness without requiring external force applicators [27]. Besides, digital image correlation has been employed to quantify displacement and strain mapping of osteocytes under shear stress [28]. Our research group has utilized partially coherent point-diffraction digital holographic microscopy (PC-pDHM) [29] to propose phase image correlation spectroscopy [30] and two-beam phase correlation spectroscopy [31] as versatile tools for quantifying the concentration, hydro-diameter, and flow velocity of transparent particles in a standard microfluidic chip. In addition, a novel computational segmentation method was proposed for tomographic phase microscopy to identify the cell nucleus in the flow cytometry mode [32]. However, to date, QPM imaging of microfluidic samples has been limited by spatial resolution, which hinders the monitoring of organelle behavior and changes in cell morphology under microfluidic stimulation without affecting the cellular state.

In this study, we present, for the first time, a high-resolution panoramic quantitative phase imaging platform based on flat-fielding quantitative phase contrast microscopy (FF-QPCM) [33]. This platform enables the capture of dynamic cell morphology and organelle behavior

under microfluidic stimulation. The self-built microchannel provides precise control over the pericellular microenvironment, while FF-QPCM offers a direct and non-invasive means of visualizing organelles in live cells with excellent quality. Thus, the proposed platform is very suitable for the systematical study on endothelial cells that are subjected to large mechanical stresses and complex microfluidic environment, providing an insight on structure and function property of cells in health and disease conditions [34–37]. With this proposed platform, we investigated the response of live COS7 cells under tuned pericellular temperature, the impact of induction duration of the oxidative phosphorylation uncoupler carbonyl cyanide m-chlorophenylhydrazone (CCCP) on mitochondria in COS7 cells, and the remarkable effects of high shear stress on live COS7 cells. We anticipate that this platform will greatly facilitate organelle-level cell biology research in the microfluidic environment.

2. Methods

2.1. High-resolution quantitative phase imaging by FF-QPCM

The proposed microfluidic stimulation and observation system consists of two main components: a high-resolution quantitative phase imaging module and a microfluidic environment control unit for live cells, as shown in Fig. 1. The high-resolution quantitative phase imaging module utilizes flat-fielding quantitative phase contrast microscopy (FF-QPCM), which is implemented on a commercial microscope body (DMi8, Leica, Germany). The schematic diagram and the real image of FF-QPCM are shown in Figs. 1(A) and 1(B), respectively. FF-QPCM is well-suited for capturing high-resolution, high-contrast, and label-free images of intracellular organelles [33]. For FF-QPCM imaging, partially coherent illuminations at different oblique angles (the angle of the illumination beam with respect to the Z axis is 45° invariably) are synchronously generated from an annular extended illuminator containing 38 LEDs (470 ± 20 nm), 50 mm above the sample plane. Such illumination design eases the installation of sample and is conducive to the enhancement of spatiotemporal resolution, spatiotemporal phase sensitivity, and optical sectioning ability. Based on the Zernike phase contrast principle, FF-QPCM generates an object wave when an illumination beam passes through the weakly scattering sample placed at the focal plane of the objective lens. This object wave consists of two components: unscattered and scattered waves. The unscattered wave that corresponds to zero-frequency components is imaged as a focused dot on the Fourier plane, while the scattered wave that corresponds to high- and low-frequency components is distributed throughout the Fourier plane. Therefore, the unscattered and scattered waves are optically separated on the Fourier plane. Overall, the unscattered and scattered waves are magnified and propagated by a confocal system composed of an oil-immersion objective lens (100×/1.44, Leica, Germany) and a tube lens (TL) to the latter's rear focal plane, which are then relayed to the working plane of a high-sensitive sCMOS camera (Zyla 4.2, Andor, UK) by a lens system L_1-L_2. Due to the identical optical path traversed by the unscattered and scattered waves, FF-QPCM is immune to environmental disturbances. The temporal resolution of FF-QPCM is 250 frames per second, providing an effective way to capture the fast dynamics of organelles. In contrast to conventional phase contrast microscopy, FF-QPCM eliminates the adverse effect of the bulk phase of the cell body on subcellular organelles by introducing synchronous phase modulation, by a phase-type spatial light modulator (SLM) (MSP1920-400-800-HSP8, Meadowlark Optics, USA), to both the unscattered wave and the low-frequency component. The phase-type SLM is conjugate to the pupil plane of the objective lens and is installed at the middle focal plane of the lens system of L_1-L_2. It is worth noting that the size of the phase modulation ring on the SLM is accurately determined in advance so that the ring covers both the zero-frequency component and the low-frequency component generated by the diffraction of bulky cell bodies on the illumination light. A quantitative phase image of the sample can be reconstructed by introducing phase shifts of 0, $\pi/2$, π, and $3\pi/2$ to the unscattered and low-frequency scattered components [33,38]. As a result, the bulky phase

distribution blurring the subcellular organelles is flattened and eliminated, making the subcellular organelles stand out and detected with high contrast in a label-free imaging manner. More details of FF-QPCM can be found in our previous work [33], in short, the phase information of a transparent sample is calculated as:

$$\varphi(\vec{r}) = a\tan\left(\frac{\beta_s(\vec{r})}{\beta_c(\vec{r}) + 2 \cdot C^2(\vec{r})}\right) + \alpha(\vec{r}), \tag{1}$$

where $\vec{r} = (x, y)$ represents the lateral vector on the sample plane, and $a\tan\{\cdot\}$ is the arctangent function. $\beta_s(\vec{r})$ and $\beta_c(\vec{r})$ are two intermediate functions related to the object wave. $C(\vec{r})$ and $\alpha(\vec{r})$ are the amplitude and phase distributions of the composite light field of unscattered wave and low-frequency scattered wave. Figures 1(C) and 1(D) show the intensity and phase images of a live COS7 cell under microfluidic stimulation within the same field of view, thereby confirming the feasibility of the proposed platform for imaging organelles in transparent live cells. As a disadvantage, FF-QPCM lacks specificity. To compensate for the disadvantage FF-QPCM is generally accompanied by a fluorescence imaging module, providing complementary information for the same sample. Also, FF-QPCM cannot directly recover the 3D refractive index (RI) distribution of the organelles, and it cannot recover the phase distribution of thick strong scattering samples due to deficiency of zero-frequency components. FF-QPCM will be further upgraded in both technology and algorithms to overcome the aforementioned drawbacks.
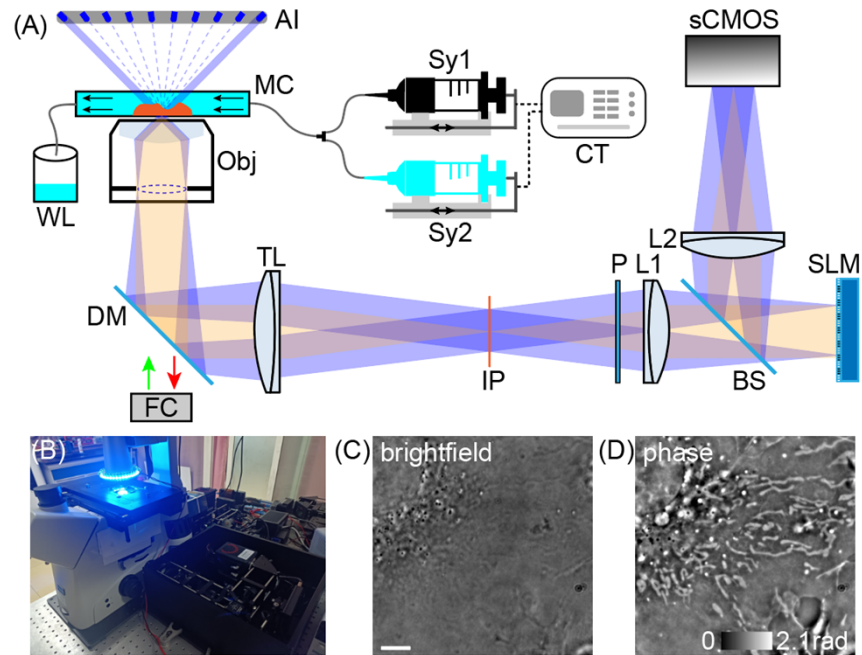

Fig. 1. High-resolution QPCM imaging of organelles in live cells under microfluidic stimulation. (A) Schematic diagram of microfluidic stimulation and observation system equipped with a microfluidic channel and flat-fielding quantitative phase contrast microscopy (FF-QPCM). (B) Real image of the experimental setup. (C) and (D) Intensity and phase images of a live COS7 cell in the same field of view. Scalebar in (C): 5 µm. AI, annular illuminator; BS, beam splitter; CT, controller; DM, dichroic mirror; FC, fluorescence channel; IP, image plane; L, lens; MC, microchannel; Obj, objective; P, polarizer; SLM, spatial light modulator; sCMOS, scientific complementary metal oxide semiconductor; Sy, syringe; TL, tube lens; WL, wasted liquid.

2.2. Fabrication of microfluidic chip for QPCM imaging

The design and fabrication of the microfluidic chip play a crucial role in controlling the pericellular environment. In this study, a specially designed microfluidic chip is utilized for both cell incubation and QPCM observation. The main components and their assembly are depicted in Fig. 2(A). The microfluidic chip consists of a 0.17 mm-thick coverslip and a 1 mm-thick glass plate for QPCM imaging purposes. The thickness of the glass plate is determined experientially to avoid fragmentation when the microfluidic chip is assembled. A microchannel with a height of 0.5 mm and a width of 5 mm is created by confining the space between the coverslip and the glass plate using a rubber with expected microchannel. The shape and size of the microchannel are designed according to application requirements and determined by fabricating a rubber along the designed position with computer numerical control (CNC) machine tools. The microchannel features two holes, serving as the inlet and outlet, respectively. These holes are connected to two rubber hoses to enable fluid flow circulation. To provide structural support, the coverslip and glass plate are held together by two mechanical shelves, which are secured using two screws, as depicted in Fig. 2(B). As a whole, our self-designed microfluidic chip can meet different application needs by expediently fabricating a rubber, and it has a very low cost compared with commercial flow chamber chips. Importantly, the coverslip is immersed in a culture medium containing suspended cells in a petri dish for cell seeding in the microchannel. The cells are then incubated for 24 hours at 37 °C and 5% CO_2. Following incubation, the coverslip is installed into the microfluidic chip for subsequent observation.
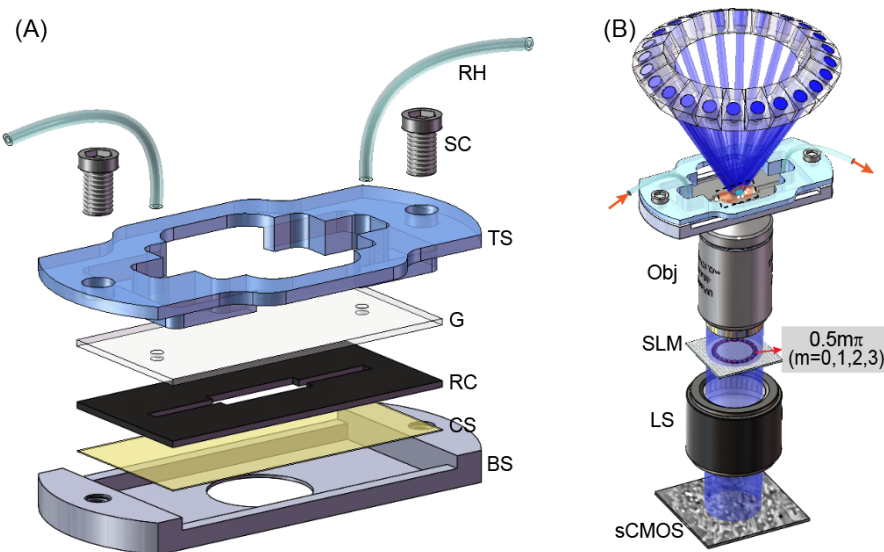

Fig. 2. Design and fabrication of microfluidic chip for high-resolution QPCM imaging of live cells. (A) Components of the microfluidic chip and their installation sequence. (B) Assembled microfluidic chip in QPCM imaging. BS, bottom shelf; CS, coverslip; G, glass; LS, lens system; Obj, objective; RC, rubber channel; RH, rubber hose; SC, screw; sCMOS, scientific complementary metal oxide semiconductor; SLM, spatial light modulator; TS, top shelf.

2.3. Sample preparation

In our study, the proposed microfluidic chip-based QPCM platform was primarily demonstrated by imaging 200-nm fluorescent polystyrene spheres and live COS7 cells under various microfluidic environments.
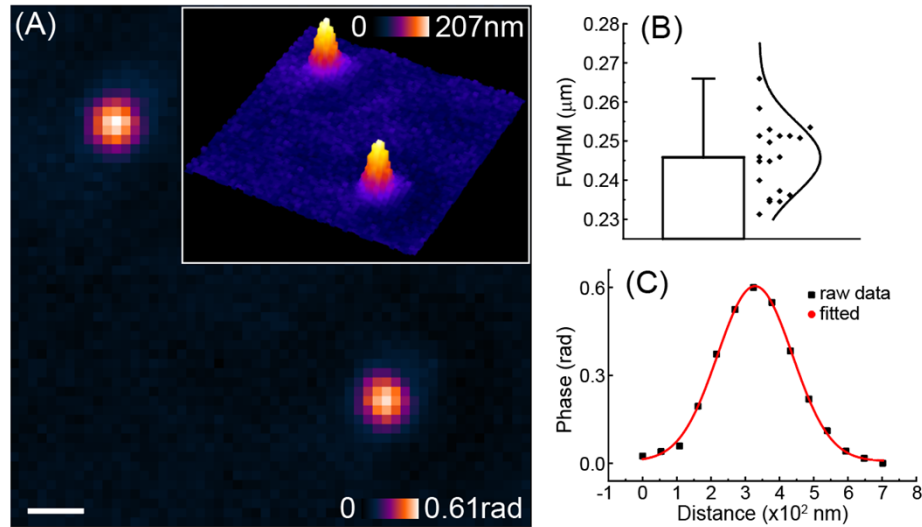
Fig. 3. Microfluidic chip-based QPCM imaging of polystyrene spheres. (A) Phase map and height distribution of 200-nm diameter polystyrene spheres reconstructed by the proposed platform. (B) FWHM statistics of the phase cut-lines crossing the centers of twenty spheres. (C) Representative phase curve crossing the center of a sphere. Scalebar in (A): 300 nm.

To prepare the polystyrene spheres, a 200-nm polystyrene spheres solution with 1% solid content (RF200C, Huge Biotechnology, China) was diluted in deionized water at a ratio of 1:3000. The mixture was then vortexed for 5 minutes at a speed of 1000 revolutions per minute. Subsequently, the solution was injected into an assembled microfluidic chip and incubated for 3 hours at room temperature. The immobilization of the polystyrene spheres onto the coverslip was achieved through a combination of gravity and electrostatic adsorption, resulting in stable attachment.

For imaging live COS7 cells in a microfluidic environment, a coverslip with a thickness of 0.17 mm was first cleaned using an ultrasonic cleaner and sterilized with ultraviolet light. A petri dish was filled with 10 mL of high glucose DMEM medium (TM 41090036, Gibco), supplemented with 10% FBS (SF0007001, HyClone) and 1% penicillin-streptomycin (J200049, HyClone). The prepared coverslip was then submerged in the culture medium, ensuring it reached the bottom of the petri dish. Fresh COS7 cells suspended in a culture medium were centrifuged and transferred into the petri dish, where they were cultured in an incubator at 37°C with 5% CO_2 for 24 hours. Before QPCM imaging, the coverslip containing the live COS7 cells was carefully removed from the petri dish and installed into the microfluidic chip. The microfluidic chip's environment was controlled by circulating different media or applying different conditions to achieve specific research objectives.

3. Results

3.1. Quantitative phase imaging of polystyrene spheres in a microfluidic chip

To verify the imaging capability of the proposed QPCM platform for live cells under microfluidic environment, a standard microfluidic sample containing 200-nm fluorescent polystyrene spheres was prepared as described in Section 2.3. The phase value induced at the center of a 200-nm polystyrene sphere was theoretically calculated as $\varphi = 2\pi \cdot [n - n_0] \cdot h / \lambda = 0.59$ rad, with $n_0 = 1.33$ being the refractive index (RI) of the deionized water, $n = 1.55$ the RI of polystyrene at the central illumination wavelength $\lambda = 470$ nm, and $h = 200$ nm the diameter of a sphere. Figure 3(A) shows

the high-contrast phase image (3D tomographic map in the upper-right corner) of the polystyrene spheres achieved using the proposed QPCM platform.

The theoretical lateral resolution of the imaging platform was estimated as $0.82 \times \lambda/$ $(NA_{illu} + NA_{det})$ with $NA_{illu} = 0.71$ and $NA_{det} = 1.44$ being the numerical aperture (NA) of the illumination beam and objective lens, and it is 179 nm. The statistical analysis for the full width at half maximum (FWHM) of twenty individual spheres was performed and shown in Fig. 3(B), revealing that the measured lateral resolution was 245.8 ± 8.9 nm (mean ± standard deviation). The measured resolution was larger than the theoretical one due to system aberrations and the non-negligible size (200 nm) of the particles. This discrepancy can be attributed to the fact that the final image is a convolution of the real size of the particles with the point spread function (PSF) of the imaging system. Figure 3(C) shows the phase distribution along a line crossing the center of a polystyrene sphere, which is well-fitted by the Gaussian function. The measured phase values at the centers of polystyrene spheres (Fig. 3(C)) were 0.61 ± 0.03 rad, corresponding to a diameter of 207 ± 10 nm at the particle centers. Therefore, the measured phase value is consistent with the theoretical one, indicating that our platform can provide accurate, high-contrast phase imaging for transparent microspheres in a microchannel.

3.2. Response of live COS7 cells to sudden temperature drop

The impact of temperature on live cells, including changes in morphology and organelle behavior, is well recognized. In our study, the microfluidic chip-based QPCM platform was employed to investigate the response of live COS7 cells to a sudden temperature drop. Live COS7 cells were prepared in a microfluidic chip following the procedure described in Section 2.3. Initially, the COS7 cells were incubated in a medium at 37°C, and the phase image of the cells in their normal state is shown in Fig. 4(A). The intracellular mitochondria and lipid droplets exhibited activity and were imaged with high contrast, as shown in Fig. 4(D). For example, a noodle-like mitochondrion indicated by a red arrow displayed deformation at one end, forming two holes and eventually adopting a doughnut shape. Moreover, a lipid droplet pointed by a green arrow exhibited close interaction with a long mitochondrion. Next, an abrupt change in the pericellular temperature was induced at a specific time t = 14.6 minutes by injecting the 4 °C medium into the microfluidic chip using a syringe. The COS7 cells exhibited a dramatic response in morphology, as shown in Fig. 4(B) and 4(C). To quantitatively analyze the response of COS7 cells to the sudden temperature drop, we measured the projected area (adhesion area) of the cells at different time points, as presented in Fig. 4(E). Prior to the injection of 4 °C medium at t = 14.6 minutes, the projected area of the cells exhibited minimal changes, with an average value of approximately 1500 μm². However, after the pericellular temperature dropped to 4 °C, the projected area of the cells significantly decreased and could be well-fitted by an exponential function. Within the first three minutes, the cells exhibited a shrinkage rate of approximately 130 μm² per minute. Subsequently, the shrinkage reached saturation as the COS7 cells adopted a spherical shape. Further details of the process can be observed in Visualization 1. Thus, by leveraging the precise temperature control offered by the microfluidic device and real-time observation facilitated by FF-QPCM, we could quantitatively assess the decay in the adhesion area of live COS7 cells in response to low-temperature stimulation.

3.3. Cell shrinkage and mitochondrial vacuolization in COS7 cells induced by continuous induction of CCCP

Mitochondrial autophagy plays a crucial role in various physiological processes such as development, cell-fate determination, and stress response [39]. The induction or inhibition of mitochondrial autophagy can be achieved using specific agents, including mitochondrial uncouplers such as carbonyl cyanide m-chlorophenylhydrazone (CCCP) and carbonyl cyanide
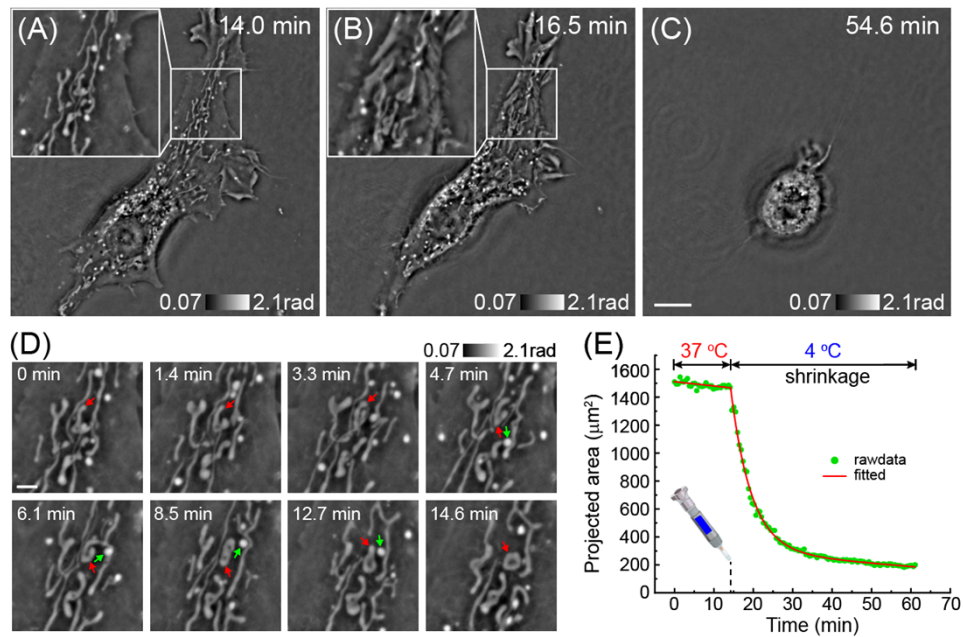
Fig. 4. Response of live COS7 cells to temperature change. The 4 °C medium was injected at 14.6 minutes. (A) Phase image of a COS7 cell when COS7 cells were incubated in 37 °C medium. (B) and (C) Phase images of the COS7 cells after the 37 °C medium was replaced with a 4 °C medium. (D) Dynamics of mitochondria and lipid droplets in a COS7 cell in 37 °C medium. (E) Adhesion area of a COS7 cell at different time points. Scalebar in (C) and (D): 10 μm and 2 μm.

p-(trifluoromethoxy)phenylhydrazone (FCCP). Among these, CCCP is an oxidative phosphorylation uncoupler that activates PINK1, leading to the phosphorylation of Parkin at Ser65 [40,41]. Previous studies have shown that induction of uncouplers for tens of minutes leads to the formation of a fraction of donut-shaped and swollen mitochondria in U2OS cells, followed by mitochondrial fragmentation after a few hours of induction [42]. However, these mitochondrial autophagy processes have primarily been observed using fluorescence microscopy, which is limited by phototoxicity and photobleaching, preventing long-term continuous observation of mitochondrial behavior. In our study, for the first time, we utilized label-free QPCM to continuously observe mitochondrial behavior under continuous CCCP induction, as depicted in Fig. 5. CCCP (HY-100941, MedChemExpress, USA) was diluted in 37 °C culture medium to a concentration of 10 μm [42]. The prepared induction solution was injected after incubating live COS7 cells in a microfluidic chip with normal medium for 14.8 minutes. During the initial 21 minutes of continuous observation (including the 14.8 minutes of incubation with a normal medium), mitochondria in COS7 cells displayed dynamic fusion and fission processes. An illustrative example is presented in Fig. 5(E). Prior to the induction of 10 μm CCCP, a mitochondrion indicated by a green arrow underwent complex deformation processes before dividing into two mitochondria. These two divided mitochondria fused back together after two minutes of induction with 10 μm CCCP. Subsequently, the fused mitochondrion became swollen and underwent further division with the assistance of a lipid droplet, as depicted in Fig. 5(E). Overall, before the induction of 10 μm CCCP, mitochondria in COS7 cells exhibited a slender, noodle-like morphology and were imaged with high contrast, as shown in Fig. 5(A). However,

under continuous induction with 10 μm CCCP, the mitochondria and cell morphology underwent significant changes.
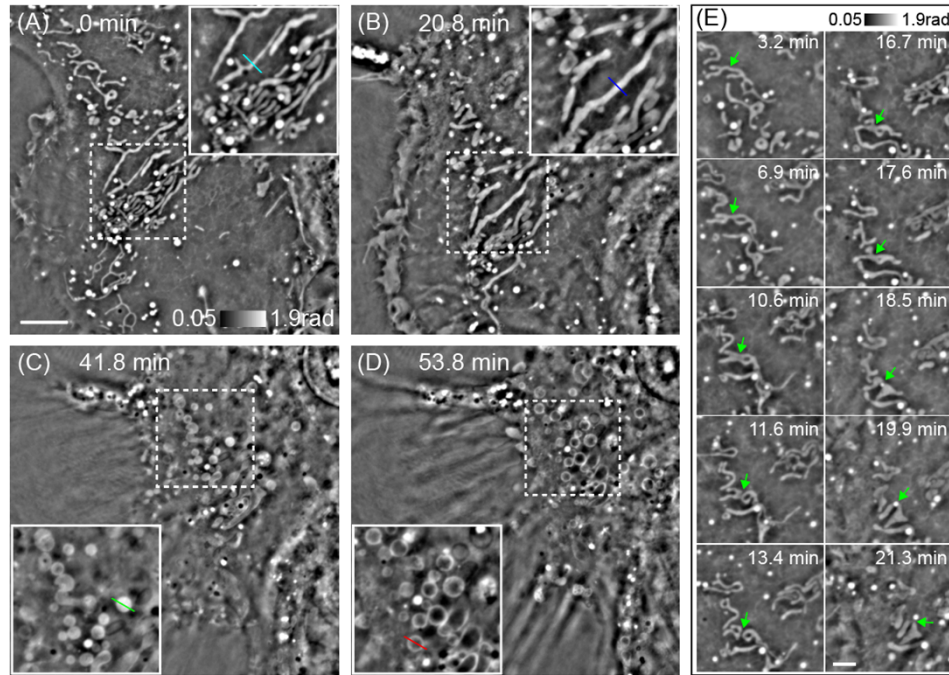

Fig. 5. Mitochondrial behavior in a live COS7 cell under the continuous induction of 10 μm CCCP. (A) Phase image of a live COS7 cell before the induction of 10 μm CCCP. (B)-(D) Phase images at different time points under the continuous induction of 10 μm CCCP. (E) Mitochondrial fusion and fission with the assistance of a lipid droplet. Scalebar in (A) and (E): 8 μm and 3 μm.

On the one hand, the long-term dynamics/states of mitochondria, including swelling (Fig. 5(B)), spheroidization (Fig. 5(C)), and vacuolization (Fig. 5(D)), could be successively observed. To quantitatively analyze the mitochondrial differences at different stages, the phase distributions along the lines crossing the representative mitochondria in Fig. 5(A)-(D) are plotted in Fig. 6(A). From the phase curves, we deduced that before the vacuolization stage, the phase value (refractive index, RI) induced by mitochondria was consistently higher than that of the surrounding cytosol, and mitochondria gradually swelled until the vacuolization stage. However, in the vacuolization stage (red line in Fig. 6(D)), most mitochondria transformed into bubble-like structures with an average thickness of 0.34 μm, and the phase value in the intermediate region was lower than the cytosol, indicating that the internal RI of mitochondria was lower than the cytosol. To quantitatively analyze the mitochondrial behavior before and after continuous induction of 10 μm CCCP, we measured the mitochondrial cross-section diameter (MCSD) and the mitochondrial contrast relative to the surrounding cytosol, as shown in Figs. 6(C) and 6(B). The mitochondrial contrast was calculated as $(\varphi_{mito}-\varphi_{cyto})/\varphi_{cyto}$ with φ_{mito} and φ_{cyto} being the average phase values induced by mitochondria and cytosol, respectively. Before the induction, mitochondria appeared slender, with an average cross-section diameter of 0.54 μm. Upon induction with 10 μm CCCP, the MCSD started to increase at a rate of 0.032 μm per minute as mitochondria swelled, as shown in Fig. 6(C). Meanwhile, the mitochondrial contrast started to drop, even below zero, during the vacuolization stage, as shown in Fig. 6(B). The most significant drop in mitochondrial contrast occurred during the swelling and vacuolization stages. The drop in contrast over the

incubation time can be fitted with a third-order polynomial function. On the other hand, COS7 cells shrank significantly 4 minutes after the induction of 10 μm CCCP. This shrinkage resulted in the production of numerous microfilaments around the cell, as shown in Fig. 6(D). And the statistical analysis in Fig. 6(D) revealed that these microfilaments had an average diameter of 300 ± 25 nm. By utilizing the microfluidic chip-assisted QPCM imaging, we achieved label-free visualization of mitochondrial vacuolization and cell shrinkage accompanied by pericellular microfilaments induced by 10 μm CCCP. More details can be found in Visualization 2.
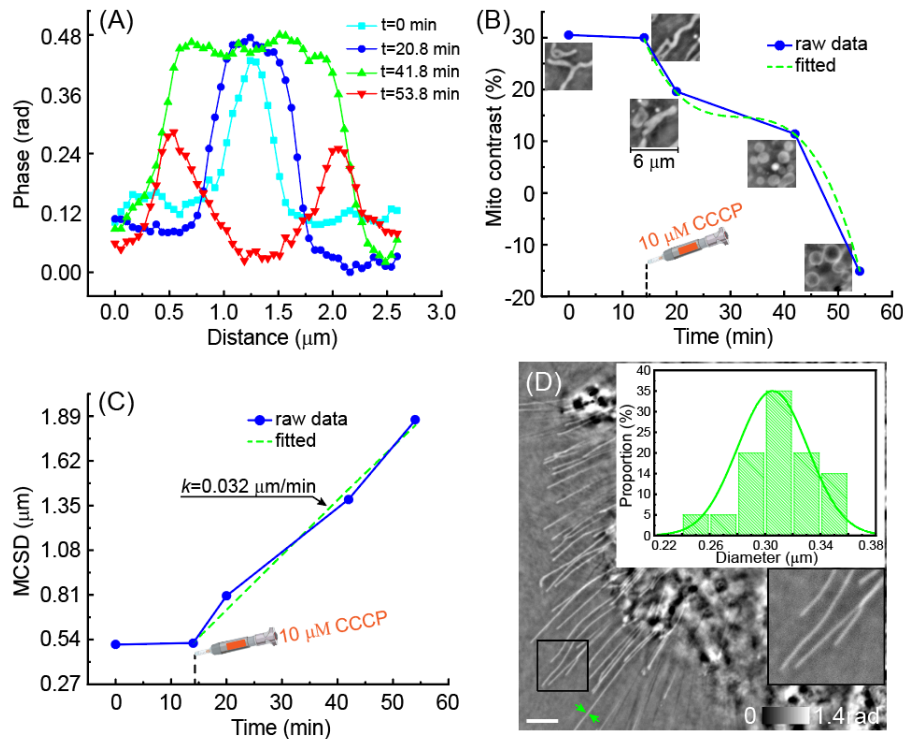

Fig. 6. Quantitative analysis when live COS7 cells were under the continuous induction of 10 μm CCCP. (A) Phase distributions along the lines crossing the representative mitochondria in Fig. 5(A)-(D). (B) Mitochondrial contrast and (C) MCSD before and after the continuous induction of 10 μm CCCP. (D) Pericellular microfilaments induced by cell shrinkage. Scalebar in (D): 5 μm.

3.4. Short-time induction of CCCP leads to temporary mitochondrial swelling and generation of VLSs in COS7 cells

Previous studies based on transmission electron microscopy (TEM) and fluorescence microscopy showed that the duration of induction with an uncoupler could lead to different mitochondrial behaviors, which are crucial for mitochondrial autophagy [39,42]. In this section, we utilized the proposed imaging platform to control the induction duration of 10 μm CCCP on live COS7 cells and observed the behaviors of intracellular organelles in a label-free manner, as depicted in Fig. 7. Similarly, a microfluidic chip containing live COS7 cells and the induction medium containing 10 μm CCCP was prepared beforehand. Initially, the live COS7 cells in the microfluidic chip were incubated with a normal medium at 37 °C for 14 minutes, during which they maintained their normal status along with the slender and noodle-like mitochondria, as shown in Fig. 7(A). Notably, various interactions occurred among organelles, such as lipid droplets assisting in

mitochondrial division (Visualization 3). Subsequently, the induction medium containing 10 μm CCCP was injected into the microfluidic chip, which was then washed out and replaced with a normal medium after 4 minutes. The mitochondrial behavior and pericellular medium at the corresponding time point are presented on the right side of Fig. 7(A). From the time series in Fig. 7(A), it can be observed that during the induction of 10 μm CCCP, the mitochondria in live COS7 cells gradually swelled, becoming shorter and larger. Interestingly, the swollen mitochondria reverted to their slender shape after injecting the normal medium. The complete dynamics can be viewed in Visualization 3. Importantly, this is the first instance of capturing the entire response of mitochondria to short-term induction with 10 μm CCCP in a label-free manner, and the observed phenomena are consistent with the reported results obtained through TEM or fluorescence microscopy [39,42]. To quantitatively characterize the mitochondrial changes throughout the observation process, we measured the mitochondrial contrast relative to the cytosol and the mitochondrial cross-section diameter (MCSD) at several representative time points, as illustrated in Figs. 7(B) and 7(C). Before the induction of 10 μm CCCP, the mitochondrial contrast remained at ∼ 38%, and the MCSD was kept at a relatively small value of ∼ 0.41 μm. However, following the injection of the induction medium, the mitochondrial contrast exhibited an average decrease of 4% per minute, and upon replacement with the normal medium, it increased at an average rate of 8% per minute, ultimately reaching the normal value of approximately 36%. Correspondingly, the MCSD increased at an average rate of 0.08 μm per minute during the induction of 10 μm CCCP, while it decreased to the normal value of approximately 0.4 μm at an average rate of 0.11 μm per minute upon injection of the normal medium. Furthermore, the COS7 cells in the microfluidic chip maintained an almost constant projected area when exposed to the normal pericellular medium at 37 °C, whereas they underwent severe shrinkage upon injection of the induction medium containing 10 μm CCCP, as depicted in Visualization 3. Quantitative analysis of mitochondrial behavior indicated that the proposed imaging platform could detect and characterize the dynamics of intracellular organelles in a controllable environment without labelling them.

In our previous work [33], we reported the detection of vesicle-like structures (VLSs) in adipose tissue-derived stem cells (ADSC). These VLSs appeared as black bubbles with an internal refractive index of 1.347 ± 0.003. Interestingly, we discovered that the short-term induction of 10 μm CCCP also resulted in the generation of VLSs in live COS7 cells, as depicted in Fig. 8. The prominent emergence of VLSs in COS7 cells was observed approximately 10 minutes after the removal of the induction medium (Visualization 3). Figure 8(A) illustrates the phase distribution of a live COS7 cell 27 minutes after the induction medium was washed out. Several organelles were identified, including the cell nucleus (CN), lipid droplets (LDs), filopodia (FP), vesicle-like structures, and mitochondria (MT). Notably, VLSs and LDs exhibit contrasting phase distributions, as demonstrated by the phase values along the green and blue lines crossing a VLS and an LD in Fig. 8(A), which are plotted in Fig. 8(B). Quantitative analysis revealed that the average diameter of VLSs was larger than that of LDs, while the maximum phase of VLSs was far below that of LDs, as shown in Fig. 8(B). Furthermore, we measured the contrast of VLSs and LDs relative to the surrounding cytosol, as shown in Fig. 8(C). The statistical results showed that the contrast of VLSs was far below zero, with a mean of -64% ± 11%, while LDs had a high contrast of 87% ± 10%. Hence, distinguishing between LDs and VLSs can be easily achieved by measuring their contrast relative to the cytosol. Additionally, we observed a tendency for fusion between VLSs, as shown in Figs. 8(D) and 8(E), consistent with the literature [33]. Overall, using high-resolution QPCM imaging of live cells in a controllable microfluidic chip, we substantiated that the short-time induction of 10 μm CCCP on live COS7 cells resulted in the temporary swelling of mitochondria and the generation of VLSs, which further validated the imaging performance of the proposed platform.
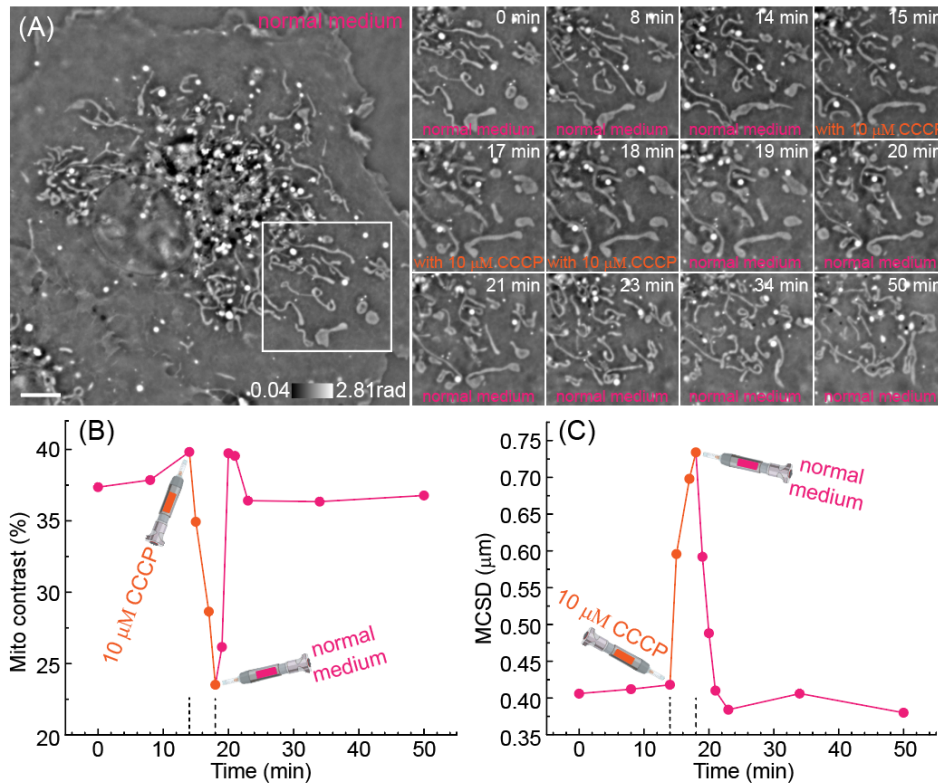
Fig. 7. Mitochondrial dynamics in a live COS7 cell mediated by 10 µm CCCP for 4 minutes. (A) Representative QPCM image of a live COS7 cell in a normal medium and the image series of mitochondria once mediated by 10 µm CCCP for 4 minutes. (B) Mitochondrial contrast and (C) MCSD during the whole observation. Scalebar in (A): 6 µm.

3.5.   *High shear stress causes directional shrinkage of COS7 cells*

Cellular mechanical properties can provide insights into the state of cells. Previous studies have used off-axis digital holographic microscopy to measure whole-cell shear stiffness under fluid shear stimulation, distinguishing between cells exposed to cytoskeletal-disrupting toxins and unexposed cells [27]. However, the subtle changes occurring at the organelle level in response to shear stress have not been reported using quantitative phase microscopy (QPM) to date. In this study, we utilize the proposed imaging platform to investigate the intriguing response of live COS7 cells to high shear stress for the first time. To apply continuous and high shear stress on cells, a peristaltic pump is employed to circulate the normal medium at a flow rate of 10 mL per minute while maintaining a temperature of 37°C. To accurately determine the flow direction of the medium within the microchannel, 5-µm polystyrene beads were diluted to an appropriate concentration and flowed at a speed of 0.26 mL per minute for objective verification. The flow direction was measured, and it was vertically upward as expected, as shown in Fig. 9. The shear stress on live cells in the microchannel was calculated using $\tau = 6\mu Q/W/h^2 = 8.6$ dyn·cm^{-2} [27,28], where $\mu = 0.0107$ dyn·s·cm^{-2} is the dynamic viscosity of the medium, $Q = 10$ mL per minute the volumetric flow rate, $W = 5$ mm the width of the flow channel, and $h = 0.5$ mm the height of the flow channel. Before a shear stress of 8.6 dyn·cm^{-2} was applied, live COS7 cells were in the normal state, including the cell morphology and mitochondrial behavior, as shown in Fig. 9(A). Surprisingly, when the shear stress was applied at 15.3 minutes, the COS7
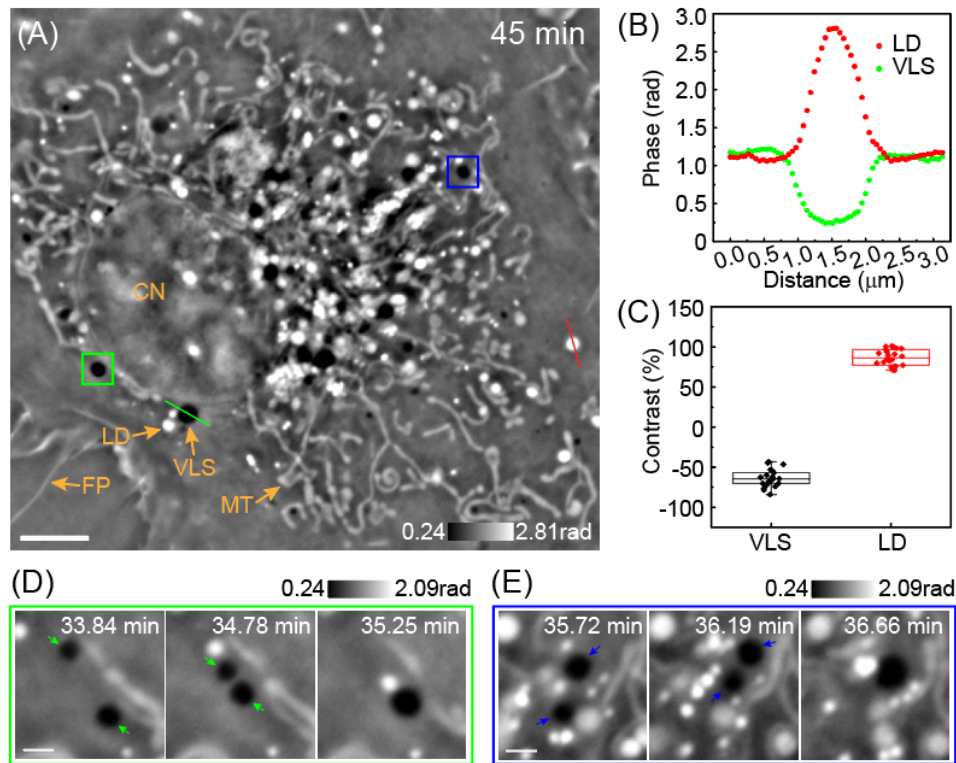
Fig. 8. Dynamics of vesicle-like structures (VLSs) in a live COS7 cell after 10 μm CCCP takes effect for 4 minutes. (A) Phase image of a live COS7 cell when 10 μm CCCP was washed out 27 minutes later. (B) Phase distributions along the red and green lines in (A). (C) Contrast statistics of VLSs and LDs relative to the cytosol. (D) Fusion of two VLSs in a green box in (A). (E) Fusion of two VLSs in a blue box in (A). Scalebar in (A), (D) and (E): 5 μm, 1 μm, and 1 μm. CN, cell nucleus; FP, filopodia; LD, lipid droplet; MT, mitochondrion; VLS, vesicle-like structure.

cells displayed different morphological changes on the oncoming and back sides of the water flow, as shown in Figs. 9(B)-9(D). The inset in Fig. 9(B) shows that the fine filopodia were distributed along the vertical upward direction, further verifying the flow direction of the medium. Under high shear stress, the COS7 cells underwent shrinkage in all directions. Specifically, the cells exhibited minimal shrinkage on the oncoming side of the water flow but significant shrinkage on the back side, as shown in Fig. 9. Interestingly, the shrinkage on the back side was implemented by the self-folding, as shown in Figs. 9(E)-9(H), the enlarged views of the white boxes in Figs. 9(A)-9(D). Meanwhile, the distribution of mitochondria on the oncoming side exhibited little influence from the shear stress, while the mitochondria on the back side were rolled up and compressed near the nucleus. The shrinkage on the back side also reduced cell adhesion strength which is proportional to the adherent area. Consequently, the adherent COS7 cells were washed away by the medium approximately 4.7 minutes after the application of shear stress. Based on estimations, the total adhesion of a COS7 cell was approximately 1.8×10^{-9} N. The entire shrinkage process can be observed in Visualization 4.

To quantitatively characterize the shrinkage behavior, we measured the shrinkage rate of the cell along different directions after the shear stress of 8.6 dyn·cm^{-2} was applied for 4.5 minutes, as shown in Fig. 10. The shrinkage rate was calculated relative to the centroid of the cell.

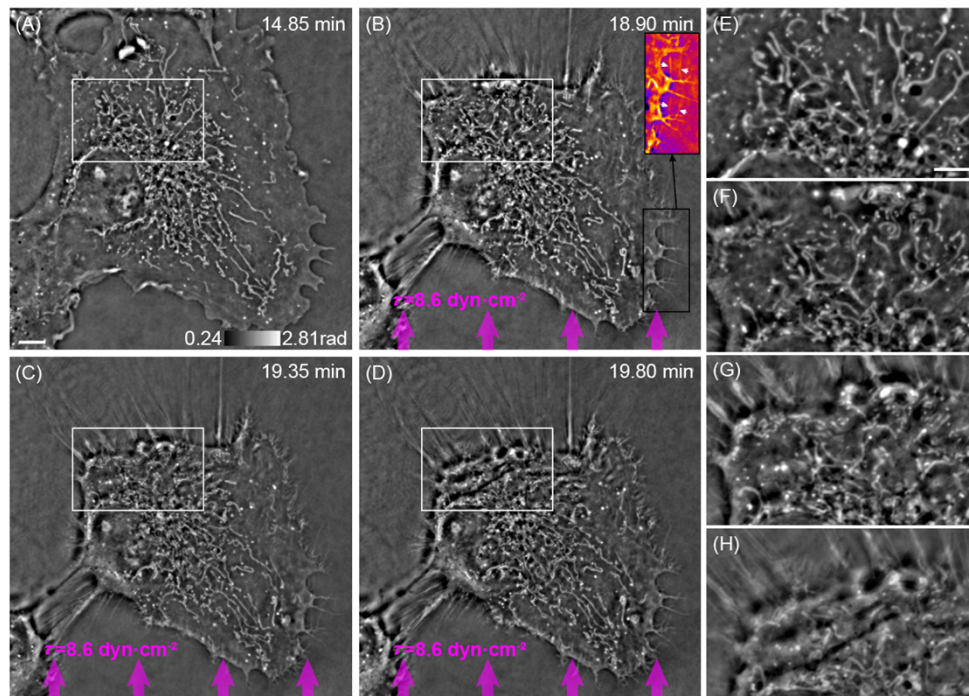**Fig. 9.** Morphology change and subcellular organelles' dynamics of a live COS7 cell when the shear stress of 8.6 dyn·cm^{-2} was applied at 15.3 minutes. (A) Phase map of a live COS7 cell before the shear stress was applied. (B)-(D) Phase images of the COS7 cell at three typical time points after the shear stress was applied. (E)-(H) Enlarged views of the white boxes in (A)-(D). Scalebar in (A) and (E): 6 μm and 4 μm.

Quantitative analysis (Fig. 10) further showed the directional dependence of cell shrinkage on the shear stress. The unique behavior exhibited by COS7 cells under shear stress was attributed to cellular mechanical properties, warranting further research to comprehend the underlying
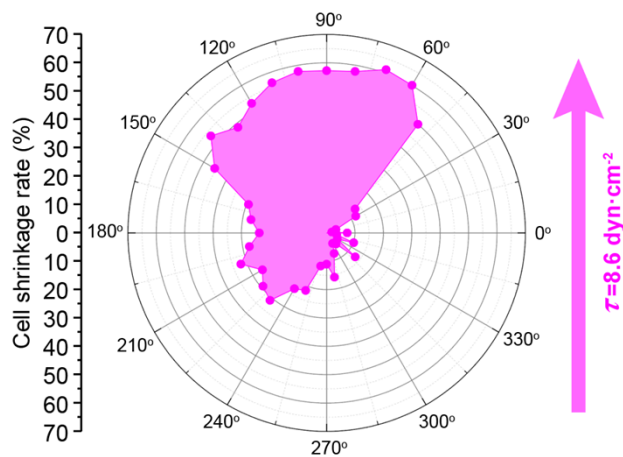

Fig. 10. Cell shrinkage rate along different directions after the shear stress of 8.6 dyn·cm^{-2} was applied for 4.5 minutes.

mechanism. It should be noted that to generate sufficient shear stress on COS7 cells within the self-built microchannel, the volumetric flow rate of the medium was set at approximately 10 mL per minute. Due to the large volumetric flow rate requirements, a peristaltic pump was utilized instead of a syringe. However, the peristalsis of the pump resulted in an erratic imaging plane during high-resolution imaging. Consequently, we only captured several phase images at selected time points under shear stress. Future improvements should focus on optimizing the microchannel size to enable the use of a controlled syringe, ensuring stable and continuous application of high shear stress on the cells.

4. Conclusion and discussion

In this paper, we introduced a label-free, high-resolution flat-fielding quantitative phase contrast microscopy combined with a microfluidic chip, which enabled the capture of cellular responses at the organelle scale under microfluidic stimulation. The FF-QPCM technique in our imaging platform allowed for high spatiotemporal resolution and enhanced imaging contrast. Concurrently, the self-designed microfluidic chip facilitated precise control over the pericellular environment. With this integrated platform, we could capture, for the first time, changes in organelles and cellular morphology in live cells when the pericellular environment was altered.

To begin, we manipulated the temperature of the pericellular environment by introducing a 4 °C medium into the microfluidic chip. QPCM imaging revealed that this low-temperature stimulation induced predictable shrinkage in the cell's projection area, which an exponential function could accurately describe. Next, we employed a mitochondrial uncoupler, 10 μm CCCP, for continuous and short-term inductions in live COS7 cells. Continuous induction led to cell shrinkage and the formation of pericellular microfilaments. Meanwhile, under continuous 10 μm CCCP induction, mitochondria exhibited three distinct states: swelling, spheroidization, and vacuolization. Each stage was characterized by different mitochondrial morphology, contrast, and mitochondrial cross-sectional diameter. Furthermore, the short-term induction of 10 μm CCCP in live COS7 cells resulted in temporary mitochondrial swelling and the generation of vesicle-like structures. A comparative analysis demonstrated that VLSs were larger and exhibited a negative contrast due to their lower refractive index than the cytosol. Additionally, the fusion between VLSs was observed. Finally, we investigated the effect of high shear stress on adherent COS7 cells. Although cell shrinkage was observed under high shear stress in all directions, the extent of shrinkage was more pronounced on the back side than on the oncoming side of the water flow. Interestingly, the shrinkage on the back side involved self-folding, with mitochondria being rolled up and squeezed, weakening cell adhesion strength. In conclusion, our study utilizing QPCM imaging of live cells within a microfluidic chip with a controllable microenvironment offers a new perspective for systematically investigating cellular responses to external stimulation at the organelle scale. Future work will focus on optimizing the microchannel parameters and fluid injection system to further enhance the performance of our imaging platform. Overall, we anticipate that this combined imaging and microfluidic stimulation platform will be valuable in life science research.

Disclosures. The authors declare no conflicts of interest.

Data availability. Data underlying the results presented in this paper are not publicly available at this time but may be obtained from the authors upon reasonable request.

References

1. X. L. Yuan, T. Darcie, Z. Y. Wei, and J. S. Aitchison, "Microchip imaging cytometer: making healthcare available, accessible, and affordable," Opto-Electron. Adv. **5**(11), 210130 (2022).
2. A. Dalili, E. Samiei, and M. Hoorfar, "A review of sorting, separation and isolation of cells and microbeads for biomedical applications: microfluidic approaches," Analyst **144**(1), 87–113 (2019).
3. S. Mao, Q. Zhang, W. Liu, Q. Huang, M. Khan, W. Zhang, C. Lin, K. Uchiyama, and J. M. Lin, "Chemical operations on a living single cell by open microfluidics for wound repair studies and organelle transport analysis," Chem. Sci. **10**(7), 2081–2087 (2019).
4. X. Zhang, D. J. Huk, Q. Wang, J. Lincoln, and Y. Zhao, "A microfluidic shear device that accommodates parallel high and low stress zones within the same culturing chamber," Biomicrofluidics **8**(5), 054106 (2014).
5. Y. Yang, Y. Li, M. Yu, C. Xue, B. Liu, Y. Wang, and K. Qin, "A passive pump-assisted microfluidic assay for quantifying endothelial wound healing in response to fluid shear stress," Electrophoresis **43**(21-22), 2195–2205 (2022).
6. K. S. Garud, S. Jeong, and M. Lee, "Computational fluid dynamics based Taguchi analysis on shear stress in microfluidic cerebrovascular channels," Int. J. Numer. Meth. Bio. **39**(7), e3733 (2023).
7. J. Na, S. Hu, C. Xue, Y. Wang, K. Chen, Y. Li, Y. Wang, and K. Qin, "A microfluidic system for precisely reproducing physiological blood pressure and wall shear stress to endothelial cells," Analyst **146**(19), 5913–5922 (2021).
8. M. Rothbauer, H. Zirath, and P. Ertl, "Recent advances in microfluidic technologies for cell-to-cell interaction studies," Lab Chip **18**(2), 249–270 (2018).
9. S. F. Berlanda, M. Breitfeld, C. L. Dietsche, and P. S. Dittrich, "Recent Advances in Microfluidic Technology for Bioanalysis and Diagnostics," Anal. Chem. **93**(1), 311–331 (2021).
10. X. W. Ou, P. Chen, and B. F. Liu, "Optical Technologies for Single-Cell Analysis on Microchips," Chemosensors **11**(1), 40 (2023).
11. Y. Guo, P. Chen, Z. Gao, Y. Li, S. Li, X. Feng, and B. F. Liu, "A time-coded multi-concentration microfluidic chemical waveform generator for high-throughput probing suspension single-cell signaling," Chin. Chem. Lett. **33**(6), 3091–3096 (2022).
12. Y. Guo, Z. Gao, Y. Liu, S. Li, J. Zhu, P. Chen, and B. F. Liu, "Multichannel synchronous hydrodynamic gating coupling with concentration gradient generator for high-throughput probing dynamic signaling of single cells," Anal. Chem. **92**(17), 12062–12070 (2020).
13. J. Qiu and F. F. Li, "Mechanical behavior of an individual adherent MLO-Y4 osteocyte under shear flow," Biomech. Model. Mechanobiol. **16**(1), 63–74 (2017).
14. S. L. Pratt, G. K. Zath, T. Akiyama, K. S. Williamson, M. J. Franklin, and C. B. Chang, "DropSOAC: Stabilizing microfluidic drops for time-lapse quantification of single-cell bacterial physiology," Front. Microbiol. **10**, 2112 (2019).
15. P. Mathur, A. F. Khartchenko, S. Stavrakis, G. V. Kaigala, and A. J. DeMello, "Quantifying antibody binding kinetics on fixed cells and tissues via fluorescence lifetime imaging," Anal. Chem. **94**(31), 10967–10975 (2022).
16. Y. K. Park, C. Depeursinge, and G. Popescu, "Quantitative phase imaging in biomedicine," Nat. Photonics **12**(10), 578–589 (2018).
17. M. Fanous, A. Keikhosravi, A. Kajdacsy-Balla, K. W. Eliceiri, and G. Popescu, "Quantitative phase imaging of stromal prognostic markers in pancreatic ductal adenocarcinoma," Biomed. Opt. Express **11**(3), 1354–1364 (2020).
18. V. Micó, J. J. Zheng, J. Garcia, Z. Zalevsky, and P. Gao, "Resolution enhancement in quantitative phase microscopy," Adv. Opt. Photonics **11**(1), 135–214 (2019).
19. T. L. Nguyen, S. Pradeep, R. L. Judson-Torres, J. Reed, M. A. Teitell, and T. A. Zangle, "Quantitative phase imaging: recent advances and expanding potential in biomedicine," ACS Nano **16**(8), 11516–11544 (2022).
20. Y. Cotte, F. Toy, P. Jourdain, N. Pavillon, D. Boss, P. Magistretti, P. Marquet, and C. Depeursinge, "Marker-free phase nanoscopy," Nat. Photonics **7**(2), 113–117 (2013).
21. D. S. Dong, X. S. Huang, L. J. Li, H. Mao, Y. Q. Mo, G. Y. Zhang, Z. Zhang, J. Y. Shen, W. Liu, Z. M. Wu, G. H. Liu, Y. M. Liu, H. Yang, Q. H. Gong, K. B. Shi, and L. Y. Chen, "Super-resolution fluorescence-assisted diffraction computational tomography reveals the three-dimensional landscape of the cellular organelle interactome," Light: Sci. Appl. **9**(1), 11–15 (2020).
22. T. H. Nguyen, M. E. Kandel, M. Rubessa, M. B. Wheeler, and G. Popescu, "Gradient light interference microscopy for 3D imaging of unlabeled specimens," Nat. Commun. **8**(1), 210 (2017).
23. X. Chen, M. E. Kandel, and G. Popescu, "Spatial light interference microscopy: principle and applications to biomedicine," Adv. Opt. Photonics **13**(2), 353–425 (2021).
24. Y. R. He, S. He, M. E. Kandel, Y. J. Lee, C. Hu, N. Sobh, M. A. Anastasio, and G. Popescu, "Cell Cycle Stage Classification Using Phase Imaging with Computational Specificity," ACS Photonics **9**(4), 1264–1273 (2022).
25. Y. Shu, J. Sun, J. Lyu, Y. Fan, N. Zhou, R. Ye, G. Zheng, Q. Chen, and C. Zuo, "Adaptive optical quantitative phase imaging based on annular illumination Fourier ptychographic microscopy," PhotoniX **3**(1), 24 (2022).
26. J. Li, A. C. Matlock, Y. Li, Q. Chen, C. Zuo, and L. Tian, "High-speed in vitro intensity diffraction tomography," Adv. Photonics **1**(06), 1 (2019).
27. W. J. Eldridge, A. Sheinfeld, M. T. Rinehart, and A. Wax, "Imaging deformation of adherent cells due to shear stress using quantitative phase imaging," Opt. Lett. **41**(2), 352–355 (2016).

28. R. Cao, W. Xiao, F. Pan, R. Tian, X. T. Wu, and L. W. Sun, "Displacement and strain mapping for osteocytes under fluid shear stress using digital holographic microscopy and digital image correlation," Biomed. Opt. Express **12**(4), 1922–1933 (2021).

29. K. Zhuo, Y. Wang, Y. Wang, K. Wen, M. Liu, Y. Ma, J. Zheng, and P. Gao, "Partially Coherent Illumination Based Point-Diffraction Digital Holographic Microscopy Study Dynamics of Live Cells," Front. Phys. **9**, 689 (2021).

30. L. Yu, Y. Wang, Y. Wang, K. Zhuo, Y. Ma, M. Liu, J. Zheng, J. L. Li, J. H. Li, and P. Gao, "Phase image correlation spectroscopy for detecting microfluidic dynamics," Appl. Opt. **61**(20), 5944–5950 (2022).

31. L. Yu, Y. Wang, Y. Wang, K. Zhuo, M. Liu, G. U. Nienhaus, and P. Gao, "Two-beam phase correlation spectroscopy: a label-free holographic method to quantify particle flow in biofluids," Photonics Res. **11**(5), 757–764 (2023).

32. D. Pirone, J. Lim, F. Merola, L. Miccio, M. Mugnano, V. Bianco, F. Cimmino, F. Visconte, A. Montella, M. Capasso, A. Iolascon, P. Memmolo, D. Psaltis, and P. Ferraro, "Stain-free identification of cell nuclei using tomographic phase microscopy in flow cytometry," Nat. Photonics **16**(12), 851–859 (2022).

33. Y. Ma, T. Q. Dai, Y. Z. Lei, J. Zheng, M. Liu, B. Sui, Z. J. Smith, K. Q. Chu, L. Kong, and P. Gao, "Label-free imaging of intracellular organelle dynamics using flat-fielding quantitative phase contrast microscopy (FF-QPCM)," Opt. Express **30**(6), 9505–9520 (2022).

34. C. A. Dessalles, C. Leclech, A. Castagnino, and A. I. Barakat, "Integration of substrate- and flow-derived stresses in endothelial cell mechanobiology," Commun. Biol. **4**(1), 764 (2021).

35. N. Nasiri-Ansari, T. Androutsakos, C. M. Flessa, I. Kyrou, G. Siasos, H. S. Randeva, E. Kassi, and A. G. Papavassiliou, "Endothelial cell dysfunction and nonalcoholic fatty liver disease (NAFLD): a concise review," Cells **11**(16), 2511 (2022).

36. D. Ogresta, A. Mrzljak, M. Cigrovski Berkovic, I. Bilic-Curcic, S. Stojsavljevic-Shapeski, and L. Virovic-Jukic, "Coagulation and endothelial dysfunction associated with NAFLD: current status and therapeutic implications," J. Clin. Transl. Hepatol. **10**(2), 339–355 (2022).

37. A. C. Peyter, J. B. Armengaud, E. Guillot, and C. Yzydorczyk, "Endothelial Progenitor Cells Dysfunctions and Cardiometabolic Disorders: From Mechanisms to Therapeutic Approaches," Int. J. Mol. Sci. **22**(13), 6667 (2021).

38. S. Wolfling, E. Lanzmann, M. Israeli, N. B. Yosef, and Y. Arieli, "Spatial phase-shift interferometry-a wavefront analysis technique for three-dimensional topometry," J. Opt. Soc. Am. A **22**(11), 2498–2509 (2005).

39. Y. Zhou, Q. Long, H. Wu, W. Li, J. Qi, Y. Wu, G. Xiang, H. Tang, L. Yang, K. Chen, L. Li, F. Bao, H. Li, Y. Wang, M. Li, and X. Liu, "Topology-dependent, bifurcated mitochondrial quality control under starvation," Autophagy **16**(3), 562–574 (2020).

40. Y. Yao, Z. Ren, R. Yang, Y. Mei, Y. Dai, Q. Cheng, C. Xu, X. Xu, S. Wang, K. M. Kim, J. H. Noh, J. Zhu, N. Zhao, Y. U. Liu, G. Mao, and J. Sima, "Salidroside reduces neuropathology in Alzheimer's disease models by targeting NRF2/SIRT3 pathway," Cell Biosci. **12**(1), 180 (2022).

41. D. Kwon, E. Park, H. Sesaki, and S. Kang, "Carbonyl cyanide 3-chlorophenylhydrazone (CCCP) suppresses STING-mediated DNA sensing pathway through inducing mitochondrial fission," Biochem. Biophys. Res. Commun. **493**(1), 737–743 (2017).

42. X. Liu and G. Hajnoczky, "Altered fusion dynamics underlie unique morphological changes in mitochondria during hypoxia–reoxygenation stress," Cell Death Differ. **18**(10), 1561–1572 (2011).